Green Chemistry

PAPER

View Article Online
View Journal | View Issue

Cite this: *Green Chem.*, 2023, **25**, 8679

Water-soluble nickel and iron salts for hydroxymethylfurfural (HMF) and water oxidation: the simplest precatalysts?†

Till Kahlstorf,‡[a] J. Niklas Hausmann,*‡[a] Indranil Mondal, [b] Konstantin Laun,[c] Ingo Zebger, [c] Tobias Sontheimer[d] and Prashanth W. Menezes *[a,b]

Received 15th June 2023,
Accepted 14th September 2023

DOI: 10.1039/d3gc02119j

rsc.li/greenchem

Electrochemical production of large-scale chemicals and fuels is critical to reaching carbon neutrality. However, the required anodic oxidation reactions, namely the oxygen evolution reaction (OER) or the oxidation of organics into value-added products, suffer from large overpotentials. To address this challenge, researchers have been widely investigating non-water-soluble (pre)catalysts to operate in the aqueous electrolyte. On the contrary, in this work, we approach a rapid, easy, and green carbon cloth electrode preparation using merely water-soluble nitrate precursors and ethanol as chemicals and no heating steps. The drop-coated, water-soluble transition metal salts reconstruct rapidly into the respective oxyhydroxides under OER conditions, with the oxyanion acting as a beneficial sacrificial reagent. This approach is shown herein for nickel(–iron) catalysts and their successful application for the OER (220 mV overpotential at 10 mA cm^{-2}, long-term stability of 40 h at 100 mA cm^{-2}) and the oxidation of 5-hydroxymethylfurfural (HMF, quantitative faradaic efficiency). We compare both reactions with both electrodes closely and find that the iron-free sample is more active for the HMF oxidation in regimes where mass transport is not the main limiting factor. We anticipate that this simple electrode preparation approach can find wide application in electrocatalysis and beyond.

Introduction

Fossil fuels and petrochemicals must be replaced by carbon-neutral alternatives to stop climate change and close the carbon cycle.[1] The most promising alternatives are hydrogen and hydrocarbons produced electrocatalytically through water or carbon dioxide reduction, respectively.[2–4] These (cathodic) reduction reactions require protons and electrons that are supplied by their (anodic) oxidative counterpart. This anodic counterpart can be the oxygen evolution reaction (OER) or an organic oxidation reaction (OOR, hybrid water splitting).[1] The OER has the advantage that only water is required as substrate; thus, it can be applied on a large scale.[1,5] However, the OER produces no value-added compound. The advantage of organic oxidation reactions is that they require thermodynamically less energy and can be value-added, *e.g.*, 5-hydroxymethylfurfural (HMF) oxidation can yield 2,5-furandicarboxylic acid (FDCA), a biomass-derived, value-added precursor for sustainable polymers.[4,6,7] However, the demand for organic oxidation products is much smaller than for hydrogen and hydrocarbon fuels.[1] Thus, the OOR can only partly replace the OER, and both reactions are crucial.[1] Nevertheless, both reactions still suffer from large overpotentials, substantially lowering the efficiency of electrolysers.[1] Thus, new catalysts that combine a high activity with a fast, green, cheap, and straightforward synthesis must be developed.

So far, a prerequisite for OER and OOR (pre)catalysts has been that they are non-water-soluble, as water is the main component of the electrolyte, leading to the potential loss of the electrodes' catalyst coating. Therefore, various non-water-soluble compounds have been investigated, such as transition metal (oxy)hydroxide,[8–10] borides,[11] pnictides,[12] chalcogenides,[13,14] alloys,[15] or intermetallics.[16–20] These

---

[a] Material Chemistry Group for Thin Film Catalysis–CatLab, Helmholtz-Zentrum Berlin für Materialien und Energie, Albert-Einstein-Str. 15, 12489 Berlin, Germany. E-mail: niklas.hausmann@helmholtz-berlin.de, prashanth.menezes@helmholtz-berlin.de
[b] Department of Chemistry: Metalorganics and Inorganic Materials, Technische Universität Berlin, Straße des 17 Juni 135, Sekr. C2, 10623 Berlin, Germany. E-mail: prashanth.menezes@mailbox.tu-berlin.de
[c] Department of Chemistry, Physical Chemistry/Biophysical Chemistry, Technische Universität Berlin, Straße des 17. Juni 135, Sekr. PC14, 10623 Berlin, Germany
[d] Strategy Department of Energy and Information, Helmholtz-Zentrum Berlin für Materialien und Energie, Hahn-Meitner-Platz 1, 14109 Berlin, Germany

† Electronic supplementary information (ESI) available: Containing all experimental procedures and characterisation details as well as additional data. See DOI: https://doi.org/10.1039/d3gc02119j

‡ These authors contributed equally to this work.

materials comprise an active site transition metal, such as iron, cobalt, or nickel, and additional constituting elements. Under alkaline OER conditions, iron, cobalt, and nickel form oxyhydroxides, and the additional constituting elements oxidise, forming oxyanions.[19,21–24] These formed oxyanions leach into the electrolyte.[13,23] Thus, the additional constituents act as a sacrificial reagent, helping to create a high surface area, defect-rich, and catalytically more active iron/cobalt/nickel oxyhydroxide phase.[13,19] Considering the inevitable and beneficial reconstruction process of the applied precatalysts, we projected that the simplest, commercially available transition metal salts, such as nitrates/sulfates/acetates, could also be suitable precatalysts, despite their water solubility, as they could rapidly reconstruct to the respective non-soluble oxyhydroxides while the anion acts as a beneficial sacrificial reagent.[25] Furthermore, such species can be dissolved and then drop-coated, enabling a simple, rapid, and reliable deposition. Such cheap, water-soluble, readily available precatalysts could enormously simplify synthesising catalysts with various transition metals, accelerating electrocatalyst development in general.

Nickel and nickel–iron are among the promising non-noble metals for the alkaline OER and OOR, making them suitable to test our water-soluble precatalyst approach.[6,15,26–31] Purely nickel-based systems are usually mediocre OER catalysts as they too strongly bind the first OER intermediate, *OH formed in the nickel(II) oxidation peak.[32–34] The addition of iron substantially improves the OER activity by shifting the *OH formation to higher energies/potentials, optimising the OER intermediate binding strengths.[32] For nickel- and nickel–iron-based catalysts, the OER and OOR share this first *OH reaction intermediate.[32,35,36] Thus, these systems can be bifunctional for both processes. While the superiority of nickel–iron-based systems for the OER is unambiguous,[37] it is controversial which system performs better for the OOR.[35,36,38–40] Some of the best OOR performances have been reported for nickel–iron-based systems.[38–41] However, other reports showed that monometallic, nickel-based systems could outperform bimetallic nickel–iron ones due to an easier formation of the *OH intermediate and a better suppression of the OER, an unwanted side reaction during OOR.[6,32,35,36,42,43] Thus, another report comparing nickel- and nickel–iron-based systems closely for the OER and OOR is valuable.

Herein, we used simple nickel and iron nitrate precursors that we dissolved in ethanol and drop-casted on a metal-free electrode substrate, carbon cloth. This approach leads to the deposition of the respective nitrates. Under OER conditions, these nitrates reconstruct within seconds into the respective oxyhydroxides. The oxyhydroxide-loaded electrodes can be rapidly prepared, their loading straightforwardly controlled, their synthesis requires no additional chemicals besides ethanol, and they achieve an excellent OER (overpotential of 220 mV at 10 mA cm^{-2}) and OOR performance (quantitative faradaic efficiency). Furthermore, we find that the nickel electrode performs better than the nickel–iron one for the OOR as it can sustain a quantitative faradaic efficiency until higher potentials and forms the reactive *OH intermediate more easily. However, in regimes where mass transport is strongly limiting, nickel- and nickel–iron-based systems can show the same conversion rate and the kinetic superiority of the monometallic nickel sample can be missed, explaining previous observations.

Results and discussion

Drop coating of the water-soluble nickel and iron nitrate salts

To realise the drop-coating of the water-soluble precursors, we choose carbon cloth as substrate, as it is transition-metal-free, cheap, conducting, comparably inert, has widely been applied for anodic oxidation reactions already, has a reasonably high surface area, and can soak in solutions.[44] As transition metal salt, we choose nickel and iron nitrate, as they are cheap, widely applied, readily available, and can be obtained in high purities. Ethanol proved to be more suitable for drop-coating than water as it evaporates more quickly, and both nitrate salts are readily soluble inside. In conclusion, this approach requires only the electrode substrate, a pipette, metal precursors, ethanol, and not a single additional chemical, binder, or machinery.[25] Furthermore, the drop coating can be performed within seconds, and no heating step is required, making this approach sustainable.[45] Additionally, in contrast to most electrodeposition approaches,[46,47] the loading can be controlled straightforwardly without using quartz microbalances, and this approach should be suitable for various transition metals, as it just requires a soluble precursor.

Fig. 1 shows in detail how the electrodes were prepared following these considerations. One electrode was drop-coated using pure nickel nitrate solution ($NiNO_3$-CC) and the other using a nickel–iron nitrate solution in a 4 : 1 molar ratio ($NiFeNO_3$-CC). $NiNO_3$-CC and $NiFeNO_3$-CC were characterised by powder X-ray diffraction (PXRD, Fig. S1) infrared (Fig. S2) and Raman spectroscopy (Fig. S3†) showing that nickel(–iron) nitrate hexahydrate formed on the carbon cloth after drying at ambient conditions.

Reconstruction to nickel(–iron) oxyhydroxides

The next step is the reconstruction of the transition metal nitrate precursors into the respective oxyhydroxides. Here, it is essential to note that the nitrate salts are water-soluble. However, in alkaline conditions, (oxy)hydroxides are thermodynamically most stable and should form over time in accordance with the Pourbaix diagrams.[48] Thus, to enable a complete and rapid reconstruction with beneficial nitrate leaching, an anodic potential of 1.63 V_{RHE} was immediately applied when the electrodes entered the 1 M KOH electrolyte (pH 13.89).[49] The current responses (Fig. S4†) show an initial peak that we assign to the precatalyst oxidation, followed by a relatively stable current that we assign to the OER. The precatalyst oxidation completes within seconds. To ensure that the material reached a steady state, we kept it for 30 min under the OER potential.

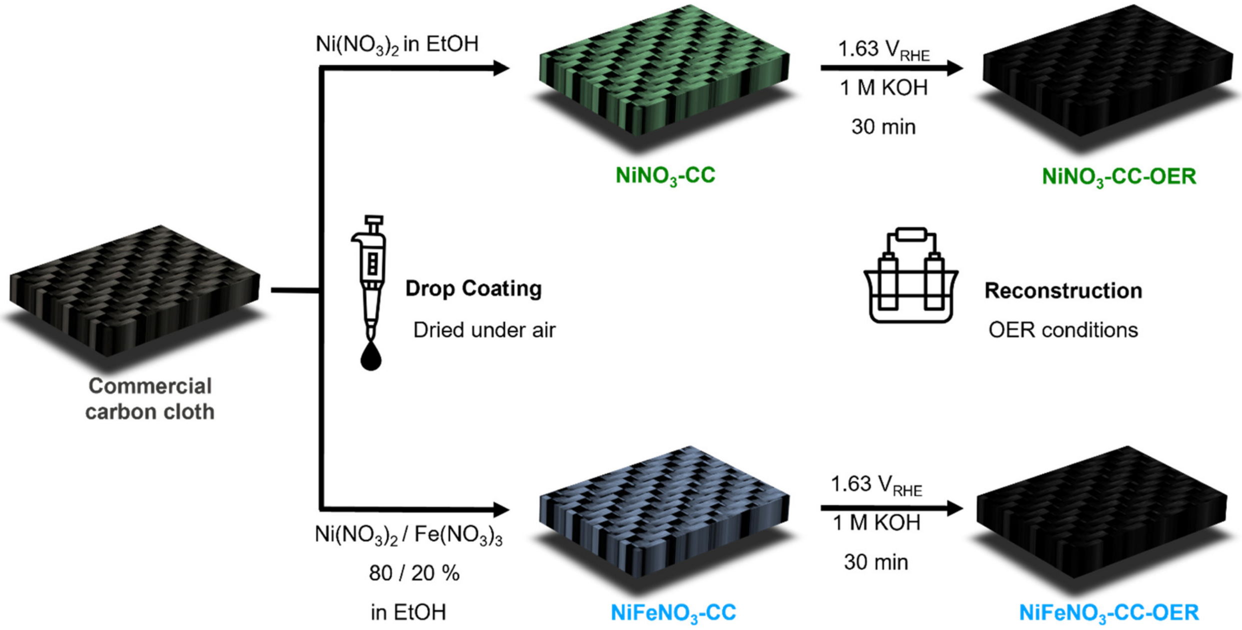

Fig. 1 Schematic illustration of the electrode preparation. Commercial carbon cloth (CC) was activated through acid treatment (HNO_3). $Ni(NO_3)_2$ and a mixture of 80% $Ni(NO_3)_2$ and 20% $Fe(NO_3)_3$ was drop coated onto the carbon cloth and the substrate was dried under air. Subsequently, the electrodes were activated at 1.63 V_{RHE} in 1.0 M KOH for 30 minutes to ensure full reconstruction into the respective oxyhydroxides.

The electrodes reconstructed for 30 min were washed with demineralised water and then characterised. These electrodes are called $NiNO_3$-CC-OER and $NiFeNO_3$-CC-OER, depending on the drop-coated transition metal. The PXRDs of both electrodes contain no sharp peaks (Fig. S1†), revealing that the crystalline nitrates have been reconstructed into X-ray amorphous phases. The infrared spectra of these amorphous phases are comparable to those of nickel(–iron) oxyhydroxides with intercalated carbonate (Fig. S2†).[50] In- and *ex situ* Raman data (Fig. 2a and d) further supports the formation of oxyhydroxides as the *in situ* Raman data shows the typical bending $\delta(M^{III}\text{-}O)$ 470 cm^{-1} and stretching $\nu(M^{III}\text{-}O)$ 566 cm^{-1} vibrations of Ni(Fe)OOH. The formation of such intercalated oxyhydroxides during OER has been widely reported in the literature.[12,23,29,51,52] For both phases, SEM-EDX mappings (Fig. 2a and b, for EDX spectra see Fig. S5 and S6†) disclose that nickel, (iron), oxygen, and potassium are homogeneously distributed. As reported previously, the potassium is most likely intercalated into the oxyhydroxide structure.[12,23,29] For both compounds, transmission electron microscopy (TEM, Fig. 2c and f) shows porous, unordered, sheetlike morphologies. Even though both compounds did not show diffraction peaks in our PXRD setup, the selected area electron diffraction (SAED) pattern reveals that both are nanocrystalline. The diffraction rings of the SAED are typical for transition metal oxyhydroxides formed during the OER.[12,53–56] The fast Fourier transforms of high-resolution TEM images confirm the lattice distances from the SAED, and the images show around 2 nm large crystallites, explaining the absence of diffraction in the PXRD. Thus, through the reconstruction of the water-soluble nitrates, porous, nanocrystalline, layered oxyhydroxides have formed.

Electrocatalytic oxygen evolution reaction (OER)

First, a loading study (0.025–4.0 mg cm^{-2}, Fig. 3a) concerning the OER activity at 400 mV overpotential (η) was conducted for $NiNO_3$-CC-OER and $NiFeNO_3$-CC-OER. For both, it shows that increasing the loading to 2 mg cm^{-2} leads to a substantial rise in the current density. Therefore, a loading of 2 mg cm^{-2} have been used throughout this manuscript. For loadings above 2 mg cm^{-2}, the current density quickly reaches a plateau, indicating a limited utilisation of the additionally loaded catalyst. Normalising the current density per loaded transition metal confirms this limited utilisation, as it keeps decreasing at higher loadings (yellow oval in Fig. 3a).

To understand this decrease in activity per loaded transition metal, we determined the number of redox-active sites, an often-used descriptor for OER active site availability.[28,35,53] The redox activity has been measured by a previously suggested potential step method (Fig. S7†) and used to normalise the current density.[57,58] The normalised current decreases initially but reaches a plateau at high loadings (3 mg cm^{-2}) together with the geometric current density (red ovals in Fig. 3a). Thus, higher loadings lead to almost no new redox active sites and simultaneously to no increase in the geometric current density. Prerequisites for redox activity and OER availability of a site are electrolyte access and electric connection to the anode. For high loadings, the additionally loaded nickel/iron sites do not fulfil these two criteria and thus cannot participate in electrocatalysis.

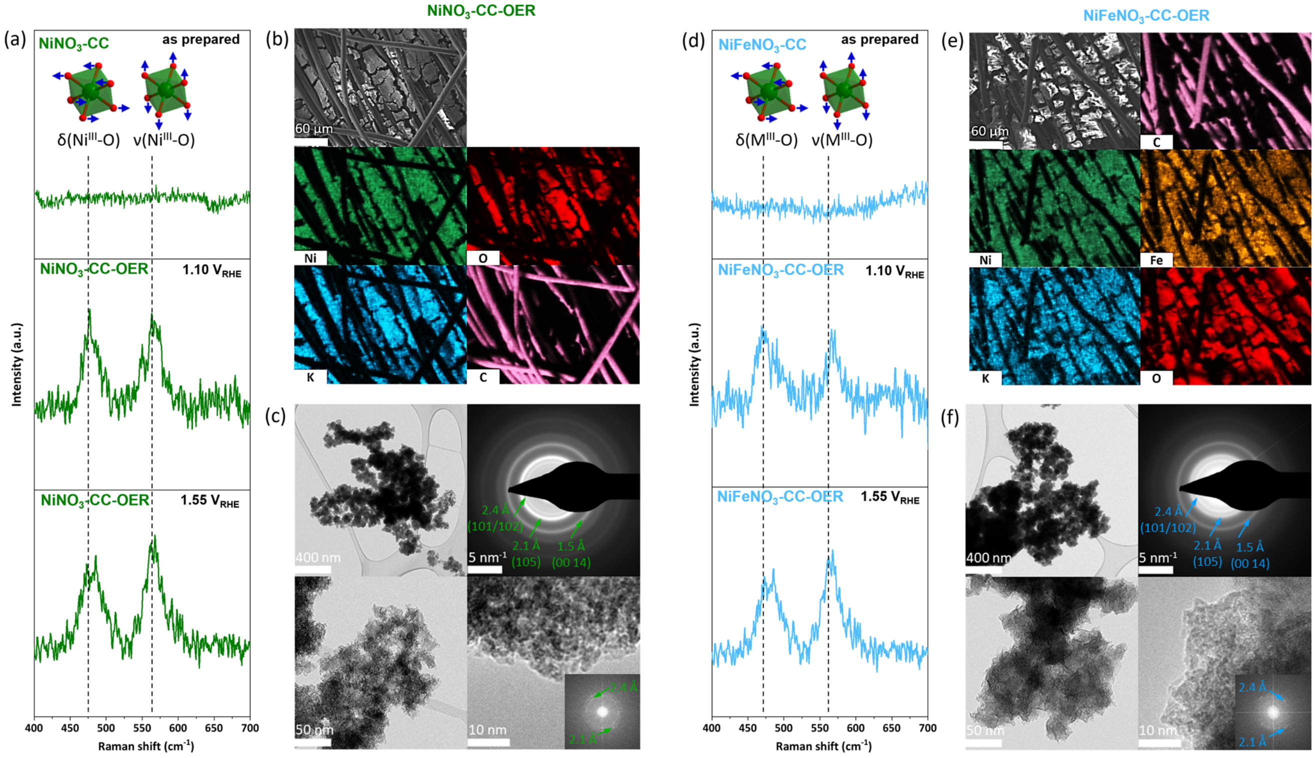

Fig. 2 (a) and (d) *in situ* Raman spectra of $NiNO_3$-CC/$NiFeNO_3$-CC and $NiNO_3$-CC-OER/$NiFeNO_3$-CC-OER (see Fig. 1 for sample abbreviations) at 1.10 V_{RHE} and 1.55 V_{RHE}, showing the formation of oxyhydroxides. The vertical dashed lines mark the prominent vibrations of the $[MO_6]$ octahedra. The spectra of the as prepared electrodes can be found in Fig. S3.† (b) SEM image of $NiNO_3$-CC-OER and SEM/EDX mapping of $NiNO_3$-CC-OER showing a homogeneous distribution of nickel and oxygen as well as the incorporation of potassium from the electrolyte during activation. The EDX spectra can for the mapping can be found in Fig. S5† (c) TEM images of $NiNO_3$-CC-OER. (e) SEM image of $NiFeNO_3$-CC-OER and SEM/EDX mapping of $NiFeNO_3$-CC-OER showing a homogeneous distribution of nickel, iron, and oxygen as well as the incorporation of potassium from the electrolyte during activation. The EDX spectra can for the mapping can be found in Fig. S6† (f) TEM images of $NiFeNO_3$-CC-OER.

We note here that double-layer capacitance measurements by cyclic voltammetry (CV) cannot be applied for these materials, as their conductivity is insufficient at potentials below the redox peak.[24,30,37,59,60] For our system, previously suggested impedance-based method were not successful, as the suggested simulation models cannot reproduce our data.[59,60]

The electrocatalytic properties towards the OER in 1 M KOH were examined for both $NiNO_3$-CC-OER and $NiFeNO_3$-CC-OER. The CV reverse scans shown in Fig. 3(b) reveal an overpotential at 10 mA cm^{-2} (η_{10}) of 290 mV for $NiNO_3$-CC-OER and 220 mV for $NiFeNO_3$-CC-OER. Both values were confirmed by chronopotentiometry measurements, maintaining these potentials for 30 minutes (Fig. S8†). These overpotentials compare favourably with previously reported ones (Table S1†). Furthermore, the incorporation of iron shifts the metal oxidation feature to higher potentials, overlapping with the onset of the OER, which has been reported previously.[28,35,61] The contribution of carbon cloth was also investigated by CV, revealing current densities below 1 mA cm^{-2} at relevant potentials (Fig. S9†). Steady-state Tafel analysis was conducted to get insights into the kinetics of the different electrodes. Fig. 3c reveals that the estimated Tafel slope of the $NiNO_3$-CC-OER electrode is 56 mV dec^{-1} and thus significantly larger than for $NiFeNO_3$-CC-OER, which is 32 mV dec^{-1}. Such a difference has already been reported for iron incorporation. It is consistent with the substantially better OER performance of the nickel–iron oxyhydroxides, where most likely edge-site, bimetallic, adjacent nickel–iron sites are responsible for the OER.[29,30,54]

We also examined the long-term stability to ensure that the simple drop-coating preparation method yielded stable electrodes. Fig. 3d reveals excellent stability over 40 hours at 100 mA cm^{-2}. After this stability test, SEM images (Fig. S10 and 11†) with elemental mappings still show a homogeneous distribution of nickel, iron, oxygen, and potassium. Furthermore, no significant change in the morphology compared to our investigations after 30 min (Fig. 2b and e) can be seen. The XRD pattern after the 40 h stability test reveals that the materials remain amorphous (Fig. S12†).

Electrocatalytic hydroxymethylfurfural (HMF) oxidation

Besides the OER, we also investigated the electrocatalytic capabilities of our drop-coated $NiNO_3$-CC-OER and $NiFeNO_3$-CC-OER electrodes towards the conversion of 5-hydroxymethylfurfural (HMF) to furan dicarboxylic acid (FDCA), a promising sustainable biopolymer building block. First, cyclic voltamme-

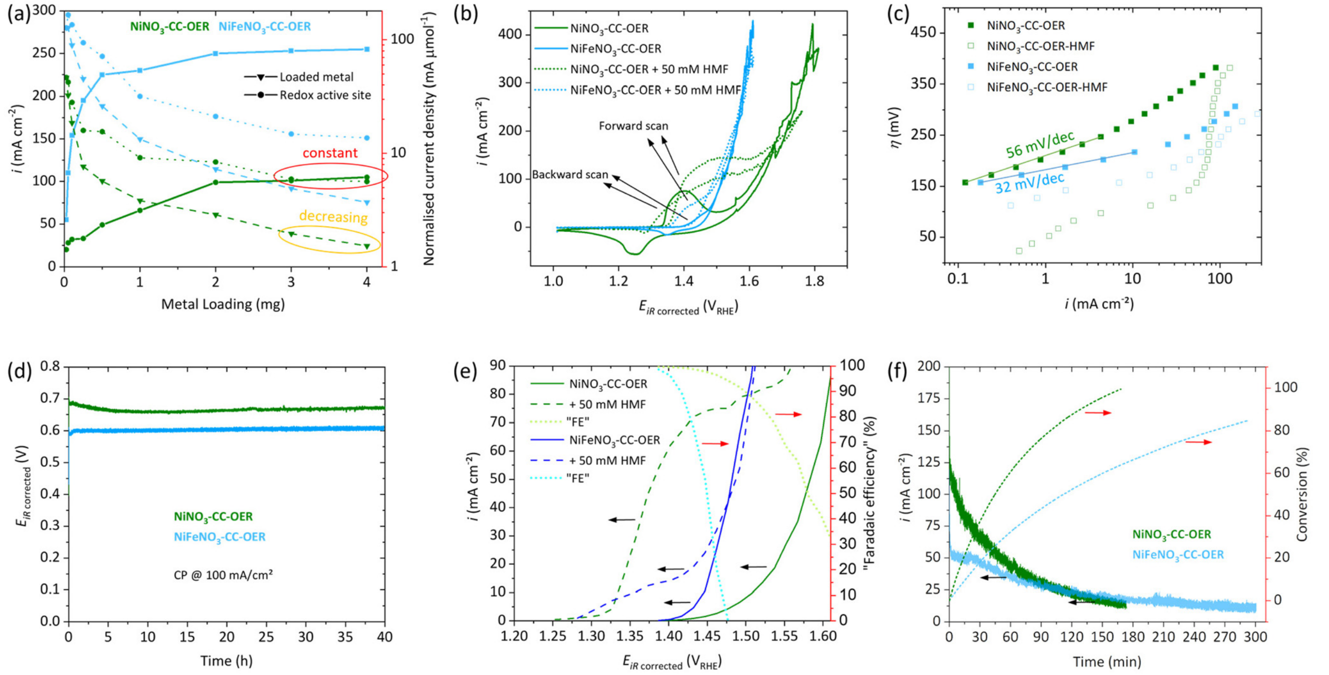

Fig. 3 Electrochemical data, all measurements were conducted in 1.0 M KOH in a three-electrode setup with platinum as the counter electrode with Hg/HgO reference. See Fig. 1 for the naming of the samples. (a) Loading study of $NiNO_3$-CC-OER (green) and $NiFeNO_3$-CC-OER (blue) per geometric current density (solid lines with squares) with normalisations per loaded metal (dashed lines with triangles) and per redox active sites (dotted lines with circles) as determined in Fig. S7.† (b) Cyclic Voltammetry of $NiNO_3$-CC-OER and $NiFeNO_3$-CC-OER at 5 mV s^{-1} with and without 50 mM HMF. (c) Tafel plots of $NiNO_3$-CC-OER and $NiFeNO_3$-CC-OER acquired through steady-state measurements. (d) 40-hour Stability measurement of $NiNO_3$-CC-OER and $NiFeNO_3$-CC-OER through chronopotentiometry at 100 mA cm^{-2}. (e) Potential *versus* current density through steady-state CA. "Faradaic efficiency" is the current portion that contributes to HMFOR at a given potential in per cent, assuming the OER current is identical with and without HMF. (f) CA data of a HMF bulk oxidation at 1.43 V_{RHE} with 600 rpm stirring conversion of HMF to FDCA on the right *y*-axis.

try was conducted in 1 M KOH electrolyte without stirring and with the addition of 50 mM HMF (Fig. 3b). For a $NiNO_3$-CC-OER, without HMF, a nickel(II) oxidation peak onsets at ~1.34 V_{RHE}; with HMF, larger current onsets around the same potential. This additional current is assigned to the oxidation of HMF.[35,38,62] In the nickel(II) oxidation peak nickel(II) is oxidised to nickel(III) and $Ni^{III+\delta}$-$O^{-II+(1-\delta)}$ (around 1.6 electrons per nickel are transferred and oxygen is redox non-innocent).[28,35,54,63,64] Two different mechanisms for the HMFOR have been proposed in the literature, depending on the applied reaction conditions and catalysts (see Fig. S13†)[6,36,40,62,65] (i) indirect oxidation, where the metal acts as a redox mediator that changes its valence state, (ii) and direct oxidation, which is potential dependent and directly oxidises HMF involving $Ni^{III+\delta}$-$O^{-II+(1-\delta)}$. Nickel-based catalysts in strongly alkaline electrolytes (pH > 13) are known to favour the indirect oxidation pathway. $Ni(OH)_2$ is oxidised to NiOOH, which is a potential-dependent step. The subsequent HMF oxidation, however, is influenced by the number of active sites that can be reduced back to $Ni(OH)_2$ and the intrinsic catalytic activity of the catalyst.[6,36,40,62,65] The enlarged oxidation peak in the forward scan of the HMF containing CVs is consistent with this hypothesis, as NiOOH is reduced to $Ni(OH)_2$ by HMF several times in the timespan of one CV resulting in multiple oxidations of the same $Ni(OH)_2$ site enlarging the nickel(II) oxidation peak. Contrary to this, the reduction peak in the back scan is less pronounced because the nickel(III) is reduced through the indirect HMF oxidation catalytic cycle, rather than the applied potential.[6] For $NiFeNO_3$-CC-OER, a similar behaviour can be observed, but the currents assigned to the oxidation peak and HMF oxidation are significantly smaller.

Fig. 3c also includes steady-state Tafel plots of the two electrodes in HMF containing 1 M KOH. HMF oxidation begins at an overpotential below 25 mV for $NiNO_3$-CC-OER, while for $NiFeNO_3$-CC-OER, it starts at 107 mV. The curves have a more complex shape than the ones in HMF-free electrolyte and lack a long linear range that could be used to unambiguously assign a Tafel slope for the HMF oxidation.

Before a closer look at the competition between the OER and HMF oxidation is taken, we investigated the effect of substrate concentration and stirring speed on the HMF oxidation. In this regard, we conducted chronoamperometry measurements (1.41 V_{RHE}) with different stirring speeds for our system. Interestingly, without stirring, $NiNO_3$-CC-OER does not outperform $NiFeNO_3$-CC-OER as both electrodes only exhibit current densities under 20 mA cm^{-2}, although one would have assumed a better performance for $NiNO_3$-CC-OER from the CVs. However, higher stirring speeds significantly increase the current density, whereby the effect is four times stronger for $NiNO_3$-CC-OER, increasing the current density from 17 mA

cm^{-2} to 100 mA cm^{-2} (Fig. S14†). For $NiFeNO_3$-CC-OER, even with rigorous stirring speeds, the current density does not increase to more than 40 mA cm^{-2}. The results highlight that mass transport limitations play a vital role for the catalytic turnover. In our unstirred system, these mass transport limitations are the decisive factor. Thus, the intrinsic activity of the catalyst cannot be measured and two catalysts with different intrinsic activities might perform similarly. However, at faster stirring speeds, the electrocatalytic activity of $NiFeNO_3$-CC-OER is limiting the overall performance, while $NiNO_3$-CC-OER's current density is substantially higher. We suggest that these mass transport limitations might be the reason why some reports have missed the superior activity of purely nickel-based systems compared to nickel–iron-based ones.

When HMF oxidation is the desired reaction, OER is an unwanted side reaction. However, at sufficiently large potential, both processes can co-occur. To investigate these two competing reactions as a function of potential, we have acquired steady-state data (3 min chronoamperometry for each data point) in stirred, HMF-free and HMF-containing 1 M KOH electrolyte (Fig. 3e). Only catalytic processes (HMF oxidation and OER) contribute to the current density of the steady-state measurements.[66] This steady-state data can be used to determine a potential at which only HMF oxidation and little OER takes place. For $NiNO_3$-CC-OER and $NiFeNO_3$-CC-OER, the HMF onset is around 1.3 V_{RHE}, and the current density increases with positive potential. Then, at higher potential, the OER starts to interfere, the range between can be considered suitable for selective HMF oxidation. For $NiNO_3$-CC-OER, this interference is less due to its 70 mV higher OER overpotential, enabling selective HMF oxidation at higher potentials and thus higher conversion rates. Additionally, using the steady-state data, we calculated and added to Fig. 3e a "faradaic efficiency" for HMF oxidation under the estimation that the OER turnover is the same with and without HMF. Consequently, Fig. 3e can be used to estimate the trade-off between turnover and faradaic efficiency for the HMF oxidation as a function of the anode potential.

Following these investigations, we choose to perform a bulk HMF oxidation with stirring and at a potential of 1.43 V_{RHE} in 1.0 M KOH with 50 mM HMF. While higher HMF concentrations are beneficial for the current density, the reaction time will also increase. As HMF is known to be unstable under strongly alkaline conditions,[67] a quick, complete conversion is vital for high yields. Furthermore, at the chosen potential, both catalysts should have a good selectivity towards HMF oxidation (Fig. 3e). $NiNO_3$-CC-OER passed the charge necessary for 100% theoretical conversion in almost half the time (170 min) of $NiFeNO_3$-CC-OER (300 min), as can be seen from Fig. 3f. Both reactions start at reasonable high current densities of 120 mA cm^{-2} and 50 mA cm^{-2}, respectively, which steadily decline until the necessary charge was passed, due to less substrate availability. The reaction mixture was investigated by ^{1}H-NMR before (Fig. S15) and after (Fig. S16 and S17†) the bulk oxidation. An internal standard was used to quantify the products and calculate the faradaic efficiencies for each catalyst. $NiNO_3$-CC-OER fully converted HMF into FDCA with a faradaic efficiency of 98%, while $NiFeNO_3$-CC-OER could only achieve 88%, indicating that the OER significantly contributed to the current density. The results fit our other findings and support that purely nickel-based systems are superior for HMF oxidation compared to those with iron incorporated.

Conclusions

We have demonstrated a rapid, simple and sustainable approach for synthesising water-soluble precursors that can be rapidly reconstructed into highly active catalysts for the oxygen evolution reaction (OER) and HMF oxidation. By drop-coating commercially available nickel and iron nitrate precursors onto carbon cloth electrodes, we achieved the deposition of the respective nitrates, which subsequently reconstructed rapidly into amorphous nickel–iron oxyhydroxide phases under OER conditions. The resulting nanocrystalline oxyhydroxide electrodes exhibited excellent OER performance, with an overpotential of 220 mV at 10 mA cm^{-2}.

The incorporation of iron in the nickel-based system shifted the oxidation of the *OH intermediate to higher energies, optimising the OER intermediate binding strengths and enhancing the OER activity. Furthermore, the nickel-based system demonstrated superior performance in the oxidation of HMF, sustaining quantitative faradaic efficiency until higher potentials and facilitating the formation of the reactive *OH intermediate. Our findings shed light on the performance comparison between nickel-based and nickel–iron-based systems for both the OER and HMFOR. While nickel–iron-based systems showed clear superiority in the OER, the OOR performance was worse. Previous reports have suggested that monometallic nickel systems could outperform bimetallic nickel–iron systems due to easier *OH intermediate formation and a better suppression of the OER during HMFOR. However, in regimes where mass transport limitations are significant, both systems may exhibit similar conversion rates, potentially overlooking the kinetic superiority of the monometallic nickel sample.

The drop-coating method utilising water-soluble precursors offers several advantages, including simplicity, a wide application range, quickness, and cost-effectiveness. It eliminates the need for additional chemicals and enables precise control over catalyst loading. Moreover, this approach can be extended to various transition metals by utilising soluble precursors, thereby accelerating the development of novel (multimetallic) catalysts for electrocatalytic conversions.

Author contributions

J. N. H. initiated the idea and developed it together with T. K. and P. W. M. T. K. prepared the electrodes, performed all electrocatalytic measurements, analysed the data. IR and TEM were measured and analysed by J. N. H. SEM experiments were conducted by I. M. K. L. and I. Z conducted *in situ* Raman experiments. T. S. helped in the investigation. T. K. and J. N. H. wrote the first draft. P. W. M. discussed the results, commented on the manuscript, and supervised the project.

Conflicts of interest

There are no conflicts to declare.

Acknowledgements

Funded by the German Federal Ministry of Education and Research (BMBF) in the framework of the project Catlab (03EW0015A/B). P. W. M. acknowledges the support from the BMBF project "PrometH2eus", 03HY105C. The authors thank Prof. Dr Matthias Driess for the infrastructure.

References

1 T. Kahlstorf, J. N. Hausmann, T. Sontheimer and P. W. Menezes, *Glob. Chall.*, 2023, 2200242.

2 R. Schlögl, *Angew. Chem., Int. Ed.*, 2019, **58**, 343–348.

3 Z. W. Seh, J. Kibsgaard, C. F. Dickens, I. Chorkendorff, J. K. Nørskov and T. F. Jaramillo, *Science*, 2017, **355**, eaad4998.

4 J. Na, B. Seo, J. Kim, C. W. Lee, H. Lee, Y. J. Hwang, B. K. Min, D. K. Lee, H.-S. Oh and U. Lee, *Nat. Commun.*, 2019, **10**, 5193.

5 J. N. Hausmann, R. Schlögl, P. W. Menezes and M. Driess, *Energy Environ. Sci.*, 2021, **14**, 3679–3685.

6 Y. Yang and T. Mu, *Green Chem.*, 2021, **23**, 4228–4254.

7 D. J. Chadderdon, L. Xin, J. Qi, Y. Qiu, P. Krishna, K. L. More and W. Li, *Green Chem.*, 2014, **16**, 3778–3786.

8 R. Gao, J. Zhu and D. Yan, *Nanoscale*, 2021, **13**, 13593–13603.

9 R. Gao and D. Yan, *Adv. Energy Mater.*, 2020, **10**, 1900954.

10 Z. Guo, W. Ye, X. Fang, J. Wan, Y. Ye, Y. Dong, D. Cao and D. Yan, *Inorg. Chem. Front.*, 2019, **6**, 687–693.

11 J. Masa, P. Weide, D. Peeters, I. Sinev, W. Xia, Z. Sun, C. Somsen, M. Muhler and W. Schuhmann, *Adv. Energy Mater.*, 2016, **6**, 1502313.

12 B. Dasgupta, J. N. Hausmann, R. Beltrán-Suito, S. Kalra, K. Laun, I. Zebger, M. Driess and P. W. Menezes, *Small*, 2023, 2301258.

13 O. Mabayoje, A. Shoola, B. R. Wygant and C. B. Mullins, *ACS Energy Lett.*, 2016, **1**, 195–201.

14 R. Gao, H. Zhang and D. Yan, *Nano Energy*, 2017, **31**, 90–95.

15 P. W. T. Lu and S. Srinivasan, *J. Electrochem. Soc.*, 1978, **125**, 265–270.

16 I. Mondal, J. N. Hausmann, G. Vijaykumar, S. Mebs, H. Dau, M. Driess and P. W. Menezes, *Adv. Energy Mater.*, 2022, **12**, 2200269.

17 J. N. Hausmann, R. Beltrán-Suito, S. Mebs, V. Hlukhyy, T. F. Fässler, H. Dau, M. Driess and P. W. Menezes, *Adv. Mater.*, 2021, **33**, 2008823.

18 C. Walter, P. W. Menezes and M. Driess, *Chem. Sci.*, 2021, **12**, 8603–8631.

19 J. N. Hausmann and P. W. Menezes, *Curr. Opin. Electrochem.*, 2022, **34**, 100991.

20 J. Masa and W. Schuhmann, *ChemCatChem*, 2019, **11**, 5842–5854.

21 B. R. Wygant, K. Kawashima and C. B. Mullins, *ACS Energy Lett.*, 2018, **3**, 2956–2966.

22 S. Jin, *ACS Energy Lett.*, 2017, **2**, 1937–1938.

23 J. N. Hausmann and P. W. Menezes, *Angew. Chem., Int. Ed.*, 2022, **61**, e202207279.

24 J. N. Hausmann, S. Mebs, H. Dau, M. Driess and P. W. Menezes, *Adv. Mater.*, 2022, **34**, 2207494.

25 G. Moon, M. Yu, C. K. Chan and H. Tüysüz, *Angew. Chem., Int. Ed.*, 2019, **58**, 3491–3495.

26 L. Trotochaud, S. L. Young, J. K. Ranney and S. W. Boettcher, *J. Am. Chem. Soc.*, 2014, **136**, 6744–6753.

27 D. A. Corrigan, *J. Electrochem. Soc.*, 1987, **134**, 377.

28 D. A. Corrigan and R. M. Bendert, *J. Electrochem. Soc.*, 1989, **136**, 723–728.

29 F. Dionigi, Z. Zeng, I. Sinev, T. Merzdorf, S. Deshpande, M. B. Lopez, S. Kunze, I. Zegkinoglou, H. Sarodnik, D. Fan, A. Bergmann, J. Drnec, J. F. de Araujo, M. Gliech, D. Teschner, J. Zhu, W.-X. Li, J. Greeley, B. R. Cuenya and P. Strasser, *Nat. Commun.*, 2020, **11**, 2522.

30 F. Dionigi, J. Zhu, Z. Zeng, T. Merzdorf, H. Sarodnik, M. Gliech, L. Pan, W. Li, J. Greeley and P. Strasser, *Angew. Chem., Int. Ed.*, 2021, **60**, 14446–14457.

31 M. Fleischmann, K. Korinek and D. Pletcher, *J. Electroanal. Chem.*, 1971, **31**, 39–49.

32 H. B. Tao, Y. Xu, X. Huang, J. Chen, L. Pei, J. Zhang, J. G. Chen and B. Liu, *Joule*, 2019, **3**, 1498–1509.

33 H. Xiao, H. Shin and W. A. Goddard, *Proc. Natl. Acad. Sci. U. S. A.*, 2018, **115**, 5872–5877.

34 A. Govind Rajan, J. M. P. Martirez and E. A. Carter, *J. Am. Chem. Soc.*, 2020, **142**, 3600–3612.

35 J. N. Hausmann, P. V. Menezes, G. Vijaykumar, K. Laun, T. Diemant, I. Zebger, T. Jacob, M. Driess and P. W. Menezes, *Adv. Energy Mater.*, 2022, 2202098.

36 N. Heidary and N. Kornienko, *Chem. Sci.*, 2020, **11**, 1798–1806.

37 M. S. Burke, S. Zou, L. J. Enman, J. E. Kellon, C. A. Gabor, E. Pledger and S. W. Boettcher, *J. Phys. Chem. Lett.*, 2015, **6**, 3737–3742.

38 P. Hauke, M. Klingenhof, X. Wang, J. F. de Araújo and P. Strasser, *Cell Rep. Phys. Sci.*, 2021, **2**, 100650, DOI: 10.1016/j.xcrp.2021.100650.

39 W.-J. Liu, L. Dang, Z. Xu, H.-Q. Yu, S. Jin and G. W. Huber, *ACS Catal.*, 2018, **8**, 5533–5541.

40 B. Mondal, N. Karjule, C. Singh, R. Shimoni, M. Volokh, I. Hod and M. Shalom, *Adv. Energy Mater.*, 2021, **11**, 2101858.

41 L. Wei, M. D. Hossain, M. J. Boyd, J. Aviles-Acosta, M. E. Kreider, A. C. Nielander, M. B. Stevens, T. F. Jaramillo, M. Bajdich and C. Hahn, *ACS Catal.*, 2023, 4272–4282.

42 B. Seo, J. Woo, E. Kim, S.-H. Cheong, D. K. Lee and H. Lee, *Catal. Commun.*, 2022, **170**, 106501.

43 L. Gouda, L. Sévery, T. Moehl, E. Mas-Marzá, P. Adams, F. Fabregat-Santiago and S. D. Tilley, *Green Chem.*, 2021, **23**, 8061–8068.

44 N. Cheng, Q. Liu, J. Tian, Y. Xue, A. M. Asiri, H. Jiang, Y. He and X. Sun, *Chem. Commun.*, 2015, **51**, 1616–1619.

45 H. C. Erythropel, J. B. Zimmerman, T. M. de Winter, L. Petitjean, F. Melnikov, C. H. Lam, A. W. Lounsbury, K. E. Mellor, N. Z. Janković, Q. Tu, L. N. Pincus, M. M. Falinski, W. Shi, P. Coish, D. L. Plata and P. T. Anastas, *Green Chem.*, 2018, **20**, 1929–1961.

46 C. G. Morales-Guio, L. Liardet and X. Hu, *J. Am. Chem. Soc.*, 2016, **138**, 8946–8957.

47 L. Trotochaud, J. K. Ranney, K. N. Williams and S. W. Boettcher, *J. Am. Chem. Soc.*, 2012, **134**, 17253–17261.

48 G. K. Schweitzer and L. L. Pesterfield, *The Aqueous Chemistry of the Elements*, Oxford University Press, Oxford, 2010.

49 J. N. Hausmann, B. Traynor, R. J. Myers, M. Driess and P. W. Menezes, *ACS Energy Lett.*, 2021, **6**, 3567–3571.

50 B. M. Hunter, W. Hieringer, J. R. Winkler, H. B. Gray and A. M. Müller, *Energy Environ. Sci.*, 2016, **9**, 1734–1743.

51 J. N. Hausmann, E. M. Heppke, R. Beltrán–Suito, J. Schmidt, M. Mühlbauer, M. Lerch, P. W. Menezes and M. Driess, *ChemCatChem*, 2020, **12**, 1161–1168.

52 J. N. Hausmann, R. A. Khalaniya, C. Das, I. Remy-Speckmann, S. Berendts, A. V. Shevelkov, M. Driess and P. W. Menezes, *Chem. Commun.*, 2021, **57**, 2184–2187.

53 J. N. Hausmann, S. Mebs, K. Laun, I. Zebger, H. Dau, P. W. Menezes and M. Driess, *Energy Environ. Sci.*, 2020, **13**, 3607–3619.

54 L. Reith, J. N. Hausmann, S. Mebs, I. Mondal, H. Dau, M. Driess and P. W. Menezes, *Adv. Energy Mater.*, 2023, **13**, 2203886.

55 P. W. Menezes, S. Yao, R. Beltrán–Suito, J. N. Hausmann, P. V. Menezes and M. Driess, *Angew. Chem., Int. Ed.*, 2021, **60**, 4640–4647.

56 K. W. Kwan, D. Xie, R. Zhang, Z. Shan and A. H. W. Ngan, *Phys. Status Solidi A*, 2018, **215**, 1800623.

57 R. D. L. Smith, C. Pasquini, S. Loos, P. Chernev, K. Klingan, P. Kubella, M. R. Mohammadi, D. Gonzalez-Flores and H. Dau, *Nat. Commun.*, 2017, **8**, 2022.

58 H. N. Nong, L. J. Falling, A. Bergmann, M. Klingenhof, H. P. Tran, C. Spöri, R. Mom, J. Timoshenko, G. Zichittella, A. Knop-Gericke, S. Piccinin, J. Pérez-Ramírez, B. R. Cuenya, R. Schlögl, P. Strasser, D. Teschner and T. E. Jones, *Nature*, 2020, **587**, 408–413.

59 S. Watzele, P. Hauenstein, Y. Liang, S. Xue, J. Fichtner, B. Garlyyev, D. Scieszka, F. Claudel, F. Maillard and A. S. Bandarenka, *ACS Catal.*, 2019, **9**, 9222–9230.

60 S. S. Jeon, P. W. Kang, M. Klingenhof, H. Lee, F. Dionigi and P. Strasser, *ACS Catal.*, 2023, **13**, 1186–1196.

61 M. B. Stevens, C. D. M. Trang, L. J. Enman, J. Deng and S. W. Boettcher, *J. Am. Chem. Soc.*, 2017, **139**, 11361–11364.

62 M. T. Bender, Y. C. Lam, S. Hammes-Schiffer and K.-S. Choi, *J. Am. Chem. Soc.*, 2020, **142**, 21538–21547.

63 D. A. Kuznetsov, B. Han, Y. Yu, R. R. Rao, J. Hwang, Y. Román-Leshkov and Y. Shao-Horn, *Joule*, 2018, **2**, 225–244.

64 M. Fleischmann, K. Korinek and D. Pletcher, *J. Chem. Soc., Perkin Trans. 2*, 1972, 1396.

65 Y. Gao, L. Ge, H. Xu, K. Davey, Y. Zheng and S.-Z. Qiao, *ACS Catal.*, 2023, 11204–11231.

66 S. Anantharaj, S. Noda, M. Driess and P. W. Menezes, *ACS Energy Lett.*, 2021, **6**, 1607–1611.

67 M. L. Krebs, A. Bodach, C. Wang and F. Schüth, *Green Chem.*, 2023, **25**, 1797–1802.